Click here to view PowerPoint presentation; Press Esc to exit

Investigating the Auroral Thermosphere with N_2^+ Lidar

Richard L. Collins, Liguo Su, Dirk Lummerzheim
Geophysical Institute
University of Alaska Fairbanks
903 Koyukuk Drive
Fairbanks, AK 99775-7320
USA

Richard A. Doe
SRI International
333 Ravenswood Avenue
Menlo Park, CA 94025-3493
USA

rlc@gi.alaska.edu / ftls1@uaf.edu / lumm@gi.alaska.edu / doe@sri.com

ABSTRACT

We present a new lidar method for investigation of the aurorally-modified ionosphere. Resonance nitrogen-ion (N_2^+ XB) lidar system is capable of making measurements of aurorally-ionized nitrogen in the polar ionosphere up to altitudes of ~300 km. We present a description of the prototype resonance lidar system that is currently being developed at Poker Flat Research Range. We compare the technical features and capabilities of this lidar system to conventional resonance lidar systems that measure atomic metals. Unlike incoherent scatter radar, the lidar measures a specific ionic species as opposed to a total ion profile. We describe how assimilative observational-modelling studies of the auroral E-region that combine measurements made with the lidar system, a radar system (i.e., the Advanced Modular Incoherent Scatter Radar), and a meridian scanning photometer with a multi-species ionospheric chemistry model will be conducted. We discuss how these observational-modelling studies will yield more accurate estimates of the ionic populations. We discuss how these studies can yield estimates of nitric oxide production while it is being created in the aurora, estimates of the auroral particle energy spectrum, and allow insights into the structure of pulsating aurora.

1.0 INTRODUCTION

The chemistry, composition, dynamics, and electrodynamics of the ionosphere (or upper mesosphere and thermosphere) are significantly influenced by the aurora [1, 2, 3]. Observations of the aurorally modified ionosphere allow insights into the composition and circulation of this region. Auroral electrons and protons are accelerated in the magnetosphere, and observations of their low altitude impact can provide significant insight into the basic neutral and ionic composition and energetics of the E-region. Specifically, auroral impact on thermospheric nitrogen creates the parent N_2^+ ion and thus feeds subsequent chemical channels to the primary E-region ions, NO^+ and O_2^+. Untangling the interplay of ionic and minor neutral composition (i.e., NO) in this chemical cascade remains one of the principle challenges in auroral aeronomy.

Collins, R.L.; Su, L.; Lummerzheim, D.; Doe, R.A. (2006) Investigating the Auroral Thermosphere with N_2^+ Lidar. In *Characterising the Ionosphere* (pp. 2-1 – 2-14). Meeting Proceedings RTO-MP-IST-056, Paper 2. Neuilly-sur-Seine, France: RTO. Available from: http://www.rto.nato.int/abstracts.asp.

Report Documentation Page

Form Approved
OMB No. 0704-0188

1. REPORT DATE	2. REPORT TYPE	3. DATES COVERED
01 JUN 2006	**N/A**	**-**

4. TITLE AND SUBTITLE	5a. CONTRACT NUMBER
Investigating the Auroral Thermosphere with N2 + Lidar	5b. GRANT NUMBER
	5c. PROGRAM ELEMENT NUMBER
6. AUTHOR(S)	5d. PROJECT NUMBER
	5e. TASK NUMBER
	5f. WORK UNIT NUMBER
7. PERFORMING ORGANIZATION NAME(S) AND ADDRESS(ES) **Geophysical Institute University of Alaska Fairbanks 903 Koyukuk Drive Fairbanks, AK 99775-7320 USA**	8. PERFORMING ORGANIZATION REPORT NUMBER
9. SPONSORING/MONITORING AGENCY NAME(S) AND ADDRESS(ES)	10. SPONSOR/MONITOR'S ACRONYM(S)
	11. SPONSOR/MONITOR'S REPORT NUMBER(S)

12. DISTRIBUTION/AVAILABILITY STATEMENT
Approved for public release, distribution unlimited

13. SUPPLEMENTARY NOTES
See also ADM002065., The original document contains color images.

14. ABSTRACT

15. SUBJECT TERMS

16. SECURITY CLASSIFICATION OF:			17. LIMITATION OF ABSTRACT	18. NUMBER OF PAGES	19a. NAME OF RESPONSIBLE PERSON
a. REPORT	b. ABSTRACT	c. THIS PAGE			
unclassified	**unclassified**	**unclassified**	**UU**	**37**	

Nitric oxide, in particular, is an ill-determined aurorally generated species which cannot be estimated by MSIS modelling. Ground-based estimates for its abundance and altitude distribution can more fully address its lifetime and role in conversion of N_2^+ to major ions. Synoptic studies of NO morphology, based on dayside satellite EUV measurements, have concluded that increases in NO at mid- and high-latitudes are associated with auroral activity [4].

Unusual brightness profiles in aurora have also been reported but remain unexplained. These include extremely thin layers (2 km) of emissions in pulsating aurora [5, 6] and enhanced layers near the lower borders of auroral curtains [7]. Determinations of the altitude and altitude extent of these sharp gradients in the auroral brightness have heretofore been made with stereoscopic optical imaging.

A plethora of observational methods exist to make auroral observations, ranging from satellites or in-situ measurements by sounding rocket to ground based remote sensing using radar and optical methods. Most observations provide line-of-sight integrated quantities, which must be supplemented by models to infer the altitude structure of the aurorally modified thermosphere. Tomographic inversions have been applied to ground based and satellite based optical observations to reconstruct the three dimensional structure with mixed success [8, 9, 10, 11, 12, 13]. Such reconstructions attempt to replicate the measurement domain of truly range-resolved diagnostics such as incoherent scatter radar (ISR) and lidars.

ISRs have been employed for over 30 years to measure ion and electron concentration, plasma temperature, and ion drift profiles in the thermosphere [14]. Altitude profiles of radar measured plasma density in the auroral E-region can be related with few assumptions to the ionization rate profile and primary electron energy spectra [15]. Although the brightness ratio of auroral emission features can be interpreted in terms of mean energy of the auroral electrons, the knowledge of the altitude profile of the excitation or ionization rate removes the uncertainty of an assumed energy distribution. Lanchester and co-workers used this method to conclude that the very intense small scale structures that are embedded in the aurora tend to be better represented by narrow Gaussian energy distributions while the surrounding less structured auroral curtain is best represented by broader Maxwellian energy distributions [16].

While ISRs unambiguously determine the electron concentration, the technique does not allow unambiguous determination of the species of ion present [6]. In order to advance our understanding for the cascade of N_2^+ to the primary E-region ions, and to characterize the interaction of ions with NO, we also require some gauge of ion composition.

Lidar techniques offer the ability to precisely measure distinct molecular species and to differentiate between the different vibrational and rotational populations that are present. The potential of lasers to probe thermospheric molecular species has been recognized since the 1960s [17]. Garner and Dao [18] presented a more detailed analysis of the problem wherein they assessed the performance of a lidar system based on current laser technology probing a 1.5-km-thick layer of aurorally-excited molecules and ions at 100 km. Collins and co-workers [19] extended these analyses to consider profiling the auroral species. These researchers surveyed the spectroscopy of molecular nitrogen and determined the optimum operational frequencies for the lidar. They then coupled photometric observations of the aurora with an ionospheric chemistry model and determined the expected profiles of several aurorally-excited species. Collins and co-workers used this analysis to establish the actual requirements for an optimum auroral lidar system. They found that the optimum lidar system was a resonance nitrogen-ion (N_2^+ XB) lidar system that would excite nitrogen ions in a single-step, $N_2^+ (X^2\Sigma^+_g (\upsilon = \upsilon_1)) \rightarrow N_2^+ (B^2\Sigma^+_u (\upsilon = \upsilon_2))$. The decay and remission would occur in a single step process (the "first negative" emission), $N_2^+ (B^2\Sigma^+_u (\upsilon = \upsilon_2)) \rightarrow N_2^+ (X^2\Sigma^+_g (\upsilon = \upsilon_3))$. A partial term diagram of molecular nitrogen is shown in Figure 1. (Note: A typo in [19] incorrectly labelled the upper state of N_2^+ as $B^3\Pi^+_u$). Finally, they presented a simulated set of observations for a night with typical

auroral activity and evaluated the performance of the resonance lidar system.

Based on the analysis of Collins and co-workers [19], we propose to conduct an assimilative observational and modelling study of the auroral thermosphere that combines measurements made with an N_2^+ XB lidar, an ISR (i.e., the Advanced Modular Incoherent Scatter Radar (AMISR)), and a meridian scanning photometer (MSP) with an ionospheric chemistry model. We show will show in Section 2 how co-volume measurement of total ion and N_2^+ density by ISR and lidar techniques, respectively, constrain a set of four aeronomical equations to predict altitude profiles for major ions NO^+ and N_2^+, as well as neutral nitric oxide. In Section 3. we discuss the specific implementation of lidar and ISR techniques required to support the model assimilation and predict the performance of the measurement ensemble. In Section 4 we discuss how the observations and modelling will be assimilated. In Section 5 we discuss the design of solid-state lidar systems for studying the vibrational population of nitrogen ions in the auroral thermosphere. In Section 6 we present our conclusions.

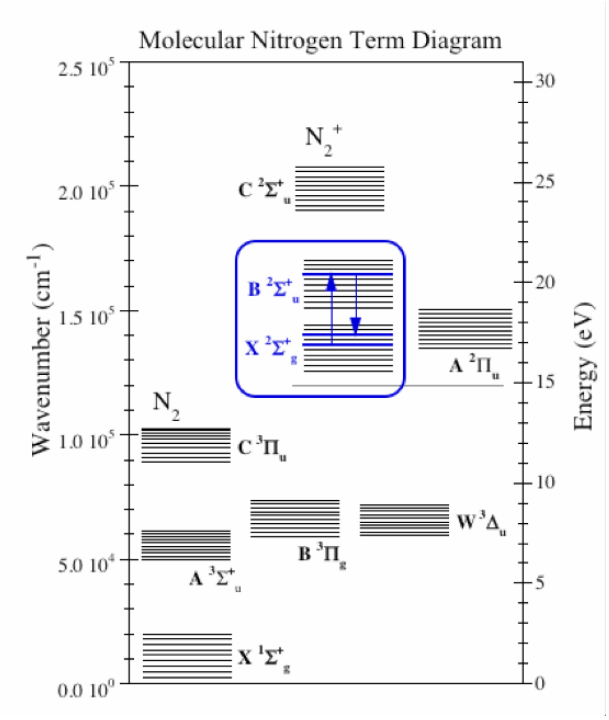

Figure 1: Partial term diagram for molecular nitrogen. The transition of interest is the first negative system; N_2^+ ($X^2\Sigma^+_g$ ($v = v_1$))→N_2^+ ($B^2\Sigma^+_u$ ($v = v_2$))→ N_2^+ ($X^2\Sigma^+_g$ ($v = v_3$)).

2.0 FRAMEWORK FOR AN ASSIMILATIVE OBSERVATIONAL AND MODELING STUDY OF THE AURORAL THERMOSPHERE

The combination of lidar and radar observations provides data which put significant constraints on ionospheric models. To demonstrate the interpretation of the data, assume a simplified ionospheric model for the auroral E-region based on the most important reactions that are listed in the appendix of Rees [2]. The N_2^+ is almost entirely produced by electron impact on neutral N_2, with a small contribution from the charge transfer reaction: $O_2^+ + N_2 \rightarrow O_2 + N_2^+$. Neglecting this reaction we still capture 90% of the ionization sources. The dominant loss processes are reactions of N_2^+ with molecular and atomic oxygen. The importance of these reactions depends on altitude. A very small fraction (about 0.1% in the auroral E-region) is lost by recombination. This leads to a simple continuity equation for the N_2^+ density. The ion-chemical processes are fast compared to the lidar measurement, and assuming steady state, the continuity equation yields:

$$\eta_{N_2^+} = \left[N_2^+\right]\left(\gamma_5\left[O_2\right] + \left(\gamma_4 + \gamma_{19}\right)[O]\right)$$

Where $\eta_{N_2^+}$ is the auroral ionization rate, square brackets denote the density of the enclosed species, and the reaction coefficients γ are those from the appendix of Rees [2]. Measuring the N_2^+ density, and taking the neutral densities from the MSIS model [20], we can directly derive the N_2^+ ionization rate as a function of altitude. The brightness of the N_2^+ first negative emission at 427.8 nm is proportional to the ionization rate, and the integrated emission is proportional to the column integrated ionization rate.

The E-region ion-chemistry for the major ions O_2^+ and NO^+ is more complicated but can also be simplified. O_2^+ has three major sources; charge transfer from N_2^+, ionization of O_2 by electron impact, and charge transfer from O^+. The latter is a small source in the E-region and can be neglected. The mechanisms by which O_2^+ is lost are dissociative recombination and reactions with NO and N_2. Assuming steady state and following the same notation as above (n_e is the electron density, α is the recombination coefficient from [2]) we get the following equation for the O_2^+ ionization rate from the continuity equation:

$$\eta_{O_2^+} + \gamma_5 \left[N_2^+ \right] \left[O_2 \right] =$$
$$\left(\gamma_{15} \left[NO \right] + \gamma_8 \left[N_2 \right] + \alpha_1 n_e \right) \left[O_2^+ \right]$$

NO^+ is produced only by chemical reactions involving N_2^+, O_2^+, O^+, the major neutrals and NO, and is lost by dissociative recombination. The steady state continuity equation yields:

$$\gamma_4 \left[N_2^+ \right] \left[O \right] + \gamma_8 \left[O_2^+ \right] \left[N_2 \right] +$$
$$\gamma_{15} \left[O_2^+ \right] \left[NO \right] =$$
$$\alpha_3 n_e \left[NO^+ \right]$$

In addition to these equations we have quasi-neutrality:

$$n_e = \left[NO^+ \right] + \left[O_2^+ \right] + \left[N_2^+ \right]$$

The lidar measures the N_2^+ density from which we derive the N_2^+ ionization rate. The radar measures the total electron density n_e. If we take the major neutral densities from MSIS, we then have three equations for the four remaining unknowns, $[O_2^+]$, $[NO^+]$, [NO], and $\eta_{O_2^+}$. The ionization cross sections for electron impact on O_2 and N_2 are similar, and the altitude profiles of the densities of these two neutral species are similar, so we may assume that the O_2 ionization rate is proportional to the N_2 ionization rate. The proportionality factor can be obtained from our auroral electron transport model and is nearly independent of altitude, which gives us the required fourth equation.

Thus combining measurements from the lidar (N_2^+), radar (n_e), and photometer (column integrated N_2^+ emission) with several assumptions (steady state, and negligible O^+ density in the E-region), we can solve this simplified E-region model and obtain the altitude profiles of the densities of the major ions (N_2^+ O_2^+ NO^+) and NO.

3.0 TECHNICAL APPROACH

3.1 Proposed N_2^+ XB Lidar System

Since 1999 an excimer-pumped dye laser has been employed as a resonance lidar transmitter at Poker Flat Research Range (PFRR), Chatanika, Alaska (65°N, 147°W). This laser system has been employed to conduct broadband measurements of the mesospheric sodium (Na) and iron (Fe) layers with 1 pm spectral resolution provided by the manufacturer [21]. The dye laser oscillator is a classic Littrow cavity that employs a rotating diffraction grating as the tuning element. In 2002 the laser grating control software system was upgraded to allow higher spectral resolution (0.1 pm) measurements of the Fe layer under operator control and make initial Fe Boltzmann lidar temperature measurements [22]. In 2004 a microprocessor-based closed-loop tuning control system was developed to allow automated high-resolution tuning of the laser [23]. Progressive

improvement of the lidar system has allowed researchers to conduct multi-year studies of the mesospheric metal layers with increasing accuracy and precision [24]. These improvements in the tuning control of the dye laser are critical for studying species that are variable in space and time and have complex molecular spectra.

To date, lidar systems at PFRR have employed telescopes with diameters of 38 cm and 60 cm. In 2003 a 1-m class (41 inches single-mirror) Cassegrain telescope was transferred from the University of Illinois at Urbana Champaign to the University of Alaska Fairbanks. The 1-m telescope will allow measurements with signals 3-7 times larger than previously attainable at PFRR. The excimer-pumped dye laser and the 1-m telescope will serve as the transmitter and receiver respectively of this new N_2^+ XB lidar system. Both the laser transmitter and telescope receiver are proven instruments and have supported a variety of lidar studies. The characteristics of the proposed system are tabulated in Table 1. The transmission and reception wavelengths have been chosen based on the spectroscopy at a temperature of 500 K. As the rotational distribution of the molecules changes with temperature the optimum lidar wavelengths change by several nanometers. The ability of the excimer-pumped dye laser to tune over relatively wide wavelength ranges is critical for this prototype lidar system to ensure that the measurements are optimized for the actual geophysical conditions.

In studies of the mesospheric Na and Fe layers, the observations are facilitated by both the relative stability of these mesospheric species and the well-defined atomic spectroscopy of Fe and Na. Thus lidar measurements of mesospheric Na and Fe can be optimized using the resonance echoes from the mesosphere. However, the aurorally produced N_2^+ layer is more variable in space and time and such operational methods cannot be relied upon. Furthermore, the standard molecular references (i.e., Iodine and Tellurium [25, 26]) do not cover the 390 nm region. The N_2^+ XB lidar system will use a standard references (e.g., stabilized HeNe laser) and a tunable Fabry Perot Interferometer as a tuning reference for the laser transmitter.

In studies of the mesospheric Na and Fe layers, where the transmission and reception wavelengths are the same (i.e., 589 nm and 372 nm respectively) the concentration of the metals is determined by taking the ratio of the resonance signal from the mesospheric metal layers to the Rayleigh signal from the stratosphere. This ratio makes the resonance lidar measurements more robust by allowing normalization of the laser power and atmospheric transmission in the lidar equation [27]. The transmission and reception resonance wavelengths in the N_2^+ XB lidar system are separated by ~ 1nm. Thus the wavelength of the Rayleigh and resonance scatter is separated by ~ 1nm. The N_2^+ XB lidar system will employ either a broadband receiver (> 1nm), a beam splitter in the receiver telescope with narrowband filters (~ 0.3 nm) for simultaneous detection of each wavelength, or a cycling approach where the lidar signal is recorded at one wavelength for a given time interval and then recorded at the other wavelength for a given time interval.

TABLE 1. Proposed N_2^+ XB Lidar System

Transmitter		Receiver	
Laser	Excimer-pumped dye	Telescope Diameter	1 m
Pulse Energy	50 mJ	Detector	Photomultiplier Tube
Pulse Repetition Rate	20 pps	Filter Bandwidth	0.3 nm
Wavelength	390.303 nm	Wavelength	391.537 nm
Measurement Resolution			
Temporal Resolution	300 s		
Spatial Resolution	5 km		

3.2 Expected Lidar Performance

Given the geophysical variability of the aurora, the performance of a given lidar system is highly dependent on the level of auroral activity. A more active aurora produces higher concentrations of excited species at lower altitudes and yields higher-quality lidar measurements, while less active aurora yield lower-quality lidar measurements. Collins and co-workers [19] reviewed two years of MSP observations and selected the night of 6-7 February 1994 (UT day 38) as representative of moderate auroral activity with varying particle characteristics. Figure 2 shows the brightness of two emission features, the "6300 line" and the "4278 band", over the course of the night. The intensity is measured in Rayleighs (R), which is used as a measure of brightness of a uniform source, such as the airglow or aurora [e.g., 3]. The aurora on the selected night is brightest early in the night (1900-2100) and just after midnight (0000-0200) when several discrete auroral arcs pass overhead from north to south and the intensity in the green line ($O(^1S) \rightarrow O(^1D)$ 557.7 nm) reaches about 100 kR. By comparison, early in the night (2100-2200) the green line intensity is about 1 kR, which is at the threshold of visual perception. One MSP channel (486.1 nm) monitors the H_β brightness, which indicates proton precipitation. The observed H_β brightness on the night of 6-7 February 1994 was insignificant, indicating that the auroral brightness was exclusively due to electron precipitation. The average N_2 ($A^3\Sigma^+_u$) and N_2^+ ($X^2\Sigma^+_g$) state concentration and temperature profiles are plotted in Figure 3. The peak concentrations and column abundances are largest (>$10^9 m^{-3}$ and ~$10^{15} m^{-2}$ respectively) when discrete auroral arcs pass overhead (1930, 0039-0200 LST). These large abundances correspond to those times when the precipitating electrons penetrate lowest into the atmosphere, and the peak of the ion layers are at their lowest altitudes. Recent satellite observations suggest that the topside N_2^+ concentrations may be significantly higher in than these model results indicate [28].

The expected lidar signal was calculated every 300s from 1902 LST to 0657 LST yielding 144 lidar signal profiles. The lidar signal profile with the largest peak amplitude at 0057 LST is plotted with the corresponding signal-to-noise-ratio (SNR) in Figure 4. The signal with the highest SNR occurs at 0057 LST during the passage of discrete auroral arcs overhead. The average signal and SNR profiles for the whole night are plotted in Figure 5. The expected lidar signal profile has an SNR greater than 10 over a range from approximately 110 to 200 km for these 300s-5 km measurements.

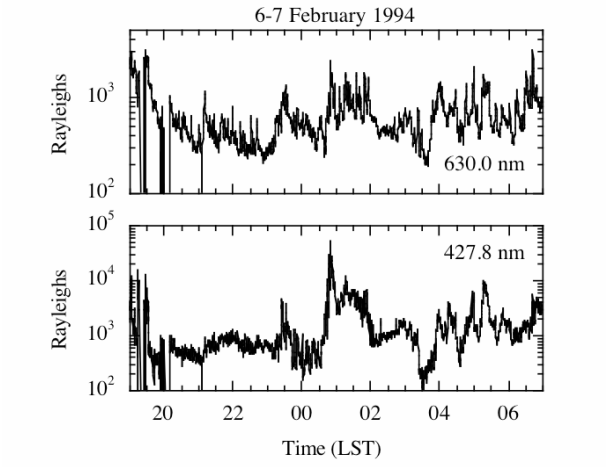

Figure 2: Meridian scanning photometer measured intensities along the magnetic zenith at 630.0 nm and 427.8 nm at Poker Flat on 6-7 February 1994. The measurements are made at 16 s intervals with a field-of-view of 1°.

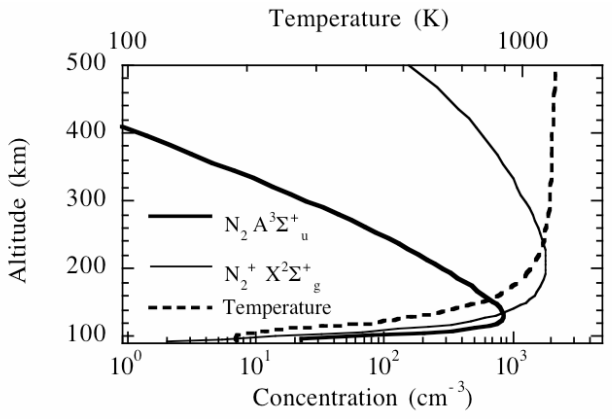

Figure 3: Average concentration profiles of $N_2(A^3\Sigma^+_u)$, N_2^+ ($X^2\Sigma^+_g$), and temperature for 6-7 February 1994. The temperature profile is taken from the MSIS model and used in deriving the concentration profiles from the MSP data in Figure 2.

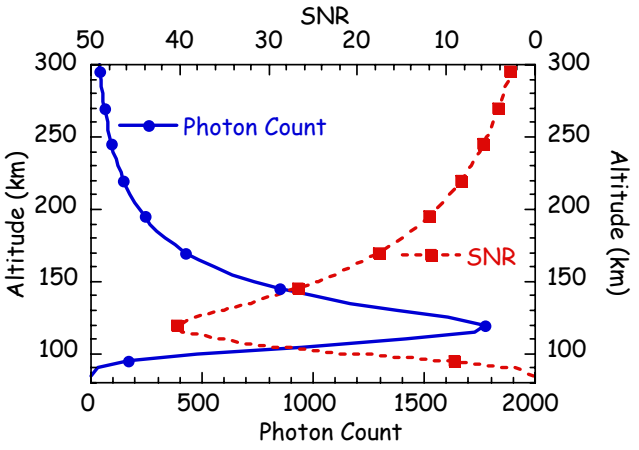

Figure 4: Expected photon count profile (solid) and signal-to-noise ratio (SNR; dashed) measured by proposed auroral lidar system during passage of auroral arcs at 0057 LST on 7 February 1994. The photon count profile represents 300s of integrated lidar echoes measured at 5 km resolution.

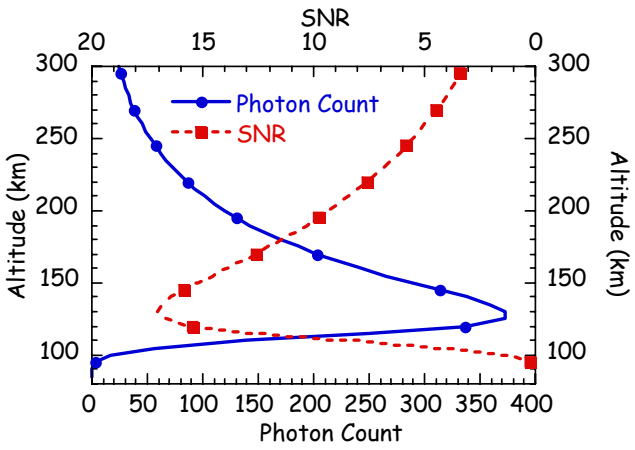

Figure 5: Expected photon count profile (solid) and signal-to-noise ratio (SNR; dashed) measured by proposed auroral lidar system averaged over whole night of 6-7 February 1994. The photon count profile represents 300s of integrated lidar echoes measured at 5 km.

The average profiles show that measurements with SNR greater than 10 occurred between 110 and 190 km. The altitude distributions of the measurement occurrence at several SNR are plotted in Figure 6. Measurements with an SNR greater than 5 are expected to be made >50% of the time at altitudes between 110 and 260 km. Measurements with an SNR greater than 10 are expected > 50% of the time over an altitude range of 120 and 180 km. Figures 4-6 highlight the potential of resonance lidar for making species specific measurements in the E- and F- Regions.

The analysis is based on lidar data acquired at a constant resolution of 300s and 5 km. In practice, the raw lidar data will be collected at a higher resolution than 300s and 5 km to allow post-measurement integration at different height and time resolutions to yield measurements with higher lower resolution and higher SNR or higher SNR and lower resolution, in order to investigate different and distinct features in the thermosphere.

3.3 Incoherent Scatter Radar Measurements

This lidar investigation will exploit the enhanced beam pointing capabilities of NSF's planned AMISR facility at PFRR. The AMISR facility establishes a new state-of-the-art for IS radar design by implementing fully electronic beam steering with a phased array of 4096 UHF transceivers. This beam pointing capability, available on a pulse-by-pulse basis, enables the formation of ionospheric plasma 'images' with temporal resolution limited by available signal SNR and desired precision in recovered plasma density and temperature estimates.

In order to address the science goals previously outlined, the AMISR will provide contextual measurements for the evolution of total ion concentration and plasma temperature for flux tubes threading the region of lidar

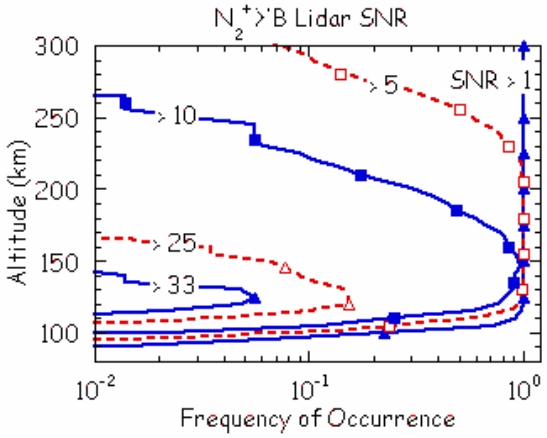

Figure 6: Expected occurrence frequency of lidar measurements of a given SNR on the night of 6-7 February 1994. Measurements with an SNR greater than 5 occur over 50% of the time over the altitude range of 120-270 km.

induced N_2^+ emission. Because the lidar beam is pointed into the zenith, as shown in Figure 6, N_2^+ backscatter from a range of altitudes maps to a spread of individual field lines. The AMISR platform is tipped 15 degrees to the magnetic north and is designed to provide beam steering over angles ±30° from boresight as indicated with gray shading in Figure 7. Thus, plasma parameters can be imaged along field lines that intersect the lidar beam over the 100 to 300 km range of altitudes predicted for N_2^+ $X^2\Sigma^+_g$ species [19]. We now address anticipated AMISR temporal and spatial sensitivity within this cone of coverage.

The AMISR has an effective aperture of 900 m^2, radiated power of 2.0 MW, a system temperature of 120 K, and a transmit duty cycle of 10%. AMISR performance can be scaled from measurements at the Sondrestrom IS radar facility by assuming that a common 320 μs coded pulse mode is employed to provide 3-km resolution in the E-region [29, 30]. Enhanced AMISR sensitivity, relative to Sondrestrom, due mainly to significantly larger antenna aperture (by a factor of 2.25) and transmitted pulse duty cycle (by a factor of 3.3), is moderated somewhat by slightly lower radiated power (by a factor of 0.8) and a slightly higher system temperature (120 K versus 85 K).

The relationship between desired precision in plasma parameters, SNR, and number of transmitted pulses has been prescribed [31]. This formula was applied to Sondrestrom for the aforementioned E-region pulse mode with assumption that plasma parameters should have no greater than 10% uncertainty. This relationship was then scaled to the AMISR system attributes and the transmitted pulse number converted to required integration time with knowledge of the interpulse period (29 ms). Figure 8 provides a nomograph for required integration time, as a function of plasma density and altitude, required to recover AMISR plasma measurements with 10% precision.

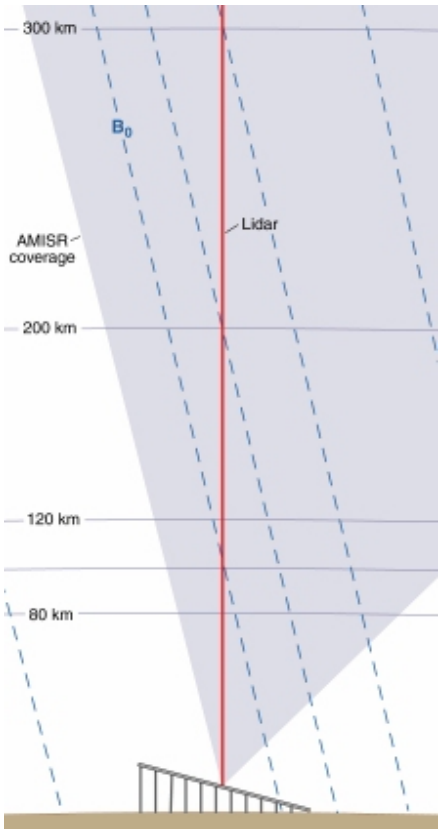

Figure 7: Viewing geometry of coordinated N_2^+ XB lidar and AMISR measurements of the aurorally modified thermosphere.

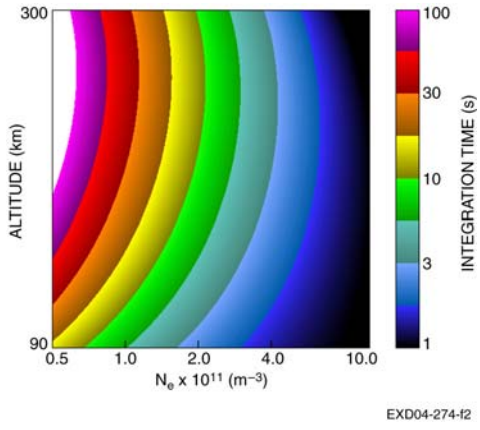

Figure 8: Nomograph for required integration time, as a function of plasma density and altitude, required to recover AMISR plasma measurements with 10% precision.

3.4 Meridian Scanning Photometer Measurements

The MSP at PFRR simultaneously records the airglow in four channels (i.e., 557.7 nm, 427.8 nm, 620.0 nm and 486.1 nm) [32]. The MSP scans along the magnetic meridian from horizon to horizon, completing a measurement every 16 seconds with a instantaneous field-of-view of 1°. Only the observations in the magnetic zenith are used as these represent the column integrated emission rates. The MSP operates in an ongoing data-logging fashion as part of the facility instrument suite at the Davis Science Center at PFRR.

4.0 COORDINATED MEASUREMENTS AND MODEL ASSIMILATION

The N_2^+ resonance lidar measurements will be nested both spatially and temporally in the AMISR and MSP measurements. The MSP provides the widest view of the thermosphere from horizon-to-horizon along the magnetic meridian every 16s. As discussed above, the resolution and accuracy of the lidar and radar Elevation scans of total plasma density measured by the ISR at the Sondrestrom Upper Atmospheric Research Facility in Kangerlussuaq, Greenland in January 2004 are plotted in Figure 9. The four panels show successive 3-minute measurements (top left, top right, bottom left, bottom right) of the total plasma density. The lower two panels show the presence of relatively stable ionization with a density of $4x10^5$ cm^{-3} at 115 km. From the nomograph in Figure 8, we see that it would take the AMISR system 2 seconds to yield a measurement profile of the total plasma density with 10% accuracy. Assuming that the concentration of N_2^+ is 1% of the total plasma density and using the analysis in Section 3.2., we expect the lidar to yield measurements of the N_2^+ profile with a resolution of 1 km and 30 seconds with 10% accuracy. Thus for the radar observations in Figure 9 we envision the following measurement strategy; during a single zenith-pointing lidar measurement we would anticipate 15 AMISR measurements of the total plasma density profile. The AMISR measurements could be made along the same direction as the lidar, however we would propose to make a set of 15 measurements that would employ the rapid electronic steering of the AMISR to yield the evolution of the spatial structure in the neighborhood (i.e., ±30° which is approximately ±60 km at 115 km)) of the lidar measurement. During the same 30 second period the MSP would yield two horizon-to-horizon scans of the airglow along the magnetic meridian providing the spatial and temporal evolution of the aurora across the sky. While the observation methodology of the MSP is fixed, we can adapt the N_2^+ resonance lidar and AMISR measurements to the specific auroral conditions. Measurements could be made at higher resolution during auroral active periods to address studies of auroral precipitation.

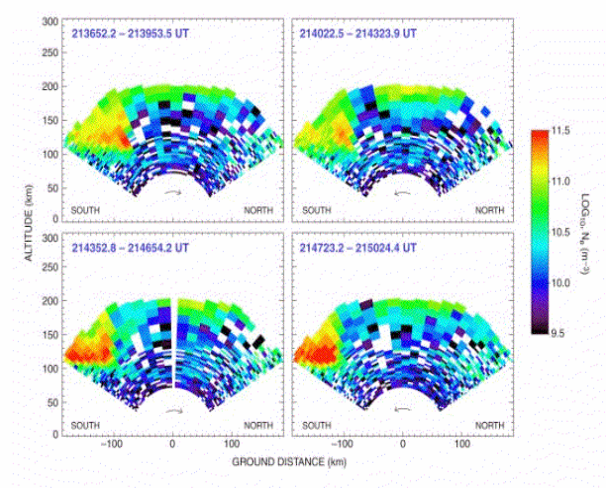

Figure 9: Elevation scans of total plasma density measured by the ISR at Sondrestrom on 18 January 2004. The panels represent successive scans taken every 3 minutes.

The coordinated lidar, radar and photometer measurements would then be used to constrain the closed set of E-region continuity equations (see Section 2) and allow determination of the ionization rates and altitude profiles of the densities of the major ions (N_2^+ O_2^+ NO^+) and NO. The development of a computationally robust and physically significant assimilation and inversion scheme is not trivial. This development will draw on analyses of the model simulations and a suite of experimental case studies that represent a range of geophysical conditions and measurement quality. The measurements of the N_2^+ profile can also be used in ISR standard inversion methods to yield estimates of the primary electron energy spectrum [15].

As we have noted in Section 3.2, during aurorally-active periods with strong auroral precipitation the N_2^+ concentrations increase and the lidar measurements will yield N_2^+ concentration profiles at higher resolution (compare SNR in Figures 4 and 5) and allow studies of the auroral precipitation.

5.0 MEASUREMENTS OF THE DISTRIBUTION OF ROTATIONAL STATES IN THE AURORA

The current study, employing a broadly tunable laser, is a first step in developing resonance lidar systems for investigating the thermosphere. To study the rotational distribution of ions in the thermosphere, a dual-laser lidar system could make simultaneous measurements of two rotational states and study the temperature distribution and thermodynamic equilibrium of the auroral thermosphere. A similar system has been employed to measure Boltzmann temperatures in the mesospheric iron layer [33]. Such a system would employ two tunable vibronic solid-state lasers (e.g., Alexandrite) that are tuned to the appropriate lines by injection seeding and frequency doubling [34]. A diagram of such a lidar system is shown in Figure 10. For example one laser could transmit at 391.081 nm ($X^2\Sigma^+_g$ (J = 0)) → $B^2\Sigma^+_\upsilon$ (J = 1)) while the other laser could transmit at 390.303 nm ($X^2\Sigma^+_g$ (J = 9)) → $B^2\Sigma^+_\upsilon$ (J = 10)). For this transmitter configuration the detectors would be tuned to 391.258 nm ($B^2\Sigma^+_\upsilon$ (J = 1) → $X^2\Sigma^+_g$ (J = 2)) and 391.537 nm ($B^2\Sigma^+_\upsilon$ (J = 10) → $X^2\Sigma^+_g$ (J = 11)) respectively. The precise choice of wavelengths could be optimised based on the expected rotational distribution of the population of molecular ions. The two lasers could be triggered alternately and so use a single receiver. Such an approach could be adapted to simplify the receiver requirements and so avoid the optical losses associated with beam splitters and the cost of multiple detectors. Such pulse-to-pulse techniques are currently employed in sodium Doppler wind temperature lidar systems [35].

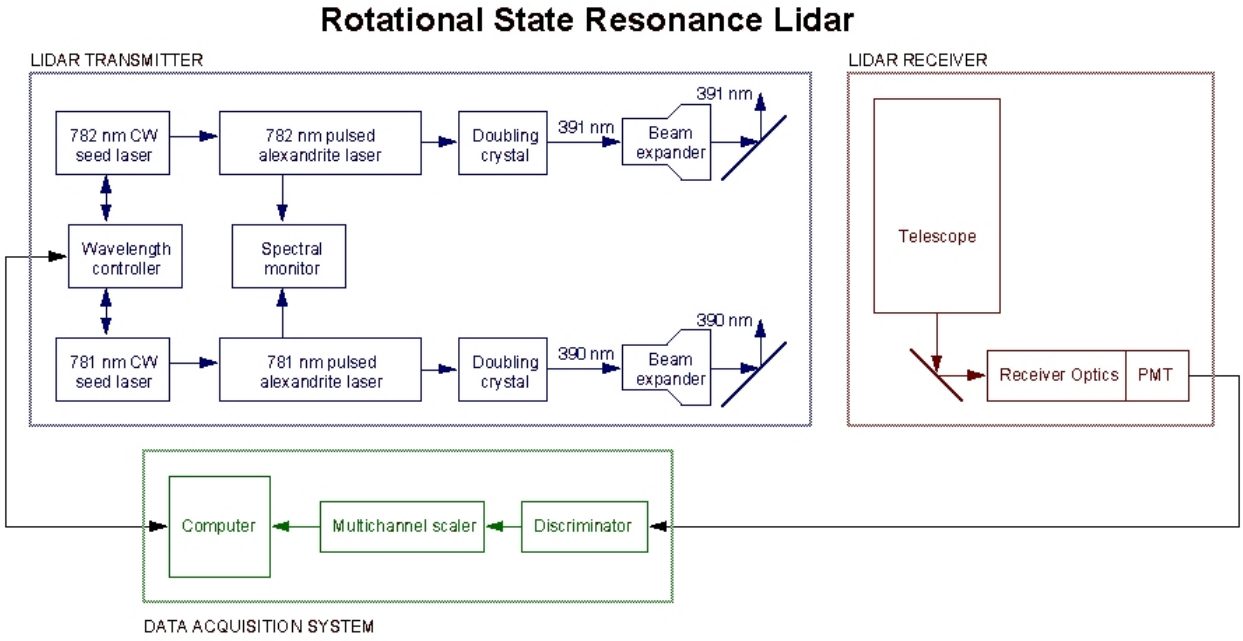

Such a system has several technical advantages over the prototype system with a single transmitter. Standard molecular spectral references can be used to stabilize the continuous wave (CW) seed lasers at 782 and 781 nm. Commercial optical materials and components are more readily available at 780 nm than at 390 nm.

6.0 CONCLUSION

In summary this paper presented the rational for the development of molecular resonance lidar systems as tools to study the auroral thermosphere. These lidars provide spectroscopic measurements of specific molecular ionic species. The combination of lidar and incoherent scatter radar measurements and assimilative models has the potential to estimate the ion composition, nitric oxide and ionisation rates in the thermosphere. A prototype N_2^+ XB lidar system that is under development at Poker Flat Research Range has been described and compared with traditional metal resonance (e.g., sodium) lidar systems. This prototype lidar system will yield measurements of at a resolution of 300s and 5 km with SNR > 10 in the 100-200 km altitude range under moderate auroral activity. More active aurora will yield higher resolution measurements over a larger altitude range. The prototype N_2^+ XB lidar system will provide scientific and engineering data for the development of dual-laser lidar systems that can measure the distribution of rotational states in aurorally ionised molecular nitrogen. These vibrational state resonance lidar will allow characterization of auroral energy deposition in the ionosphere.

7.0 REFERENCES

[1] Vallance Jones, A., 1974, *Aurora*, Reidel, Dordrecht.

[2] Rees, MH, 1989. *Physics and chemistry of the upper atmosphere*, Cambridge University Press, Cambridge.

[3] Chamberlain, JW, 1995. Physics of the Aurora and the Airglow, *American Geophysical Union,* Washington.

[4] Barth, CA, KD Mankoff, SM Bailey, and SC Solomon, 2003. Global observations of nitric oxide in the thermosphere, *J. Geophys. Res., 108*(A1), 1027, doi:10.1029/2002JA009458.

[5] Stenbaek-Nielsen, HC and TJ Hallinan, 1979. Pulsating auroras - Evidence for noncollisional thermalization of precipitating electrons, *J. Geophys. Res., 84*, 3257.

[6] Wahlund, J-E, HJ Opennoorth, and P Rothwell, 1989. Observations of thin auroral ionization layers by EISCAT in connection with pulsating aurora, *J. Geophys. Res., 94,* 17,223-17,233.

[7] Hallinan, TJ, HC Stenbaek-Nielsen, and CS Deehr, 1985. Enhanced aurora, *J. Geophys. Res., 90*, 8461.

[8] Solomon, SC, PB Hays, and VJ Abreu, 1988. The auroral 6300 A emission - Observations and modeling, *J. Geophys. Res., 93*, 9867.

[9] McDade, IC and EJ Llewellyn, 1991. Inversion techniques for recovering two-dimensional distributions of auroral emission rates from tomographic rocket photometer measurements, *Can. J. Phys., 69*, 1059.

[10] Vallance Jones, A, RL Gattinger, F Creutzberg, FR Harris, AG McNamara, AW Yau, EJ Llewellyn, D Lummerzheim, MH Rees, IC McDade, and J Margot, 1991. The ARIES Auroral Modelling Campaign: Characterization and Modelling of an Evening Auroral Arc Observed from a Rocket and a Ground-based Line of Meridian Scanners, *Planet. Space Sci., 39*, 1677.

[11] Frey, S, HU Frey, DJ Carr, OH Bauer, G Haerendel, 1996. Auroral emission profiles extracted from three-dimensionally reconstructed arcs, *J. Geophys. Res., 101,* 21,731.

[12] Doe, RA, JD Kelly, JL Semeter, and DP Steele, 1997. Tomographic reconstruction of 630.0 nm emission structure for a polar cap arc, *Geophys. Res. Lett., 24*, 1119.

[13] Semeter, J, M Mendillo, and J Baumgardner, 1999. Multispectral tomographic imaging of the midlatitude aurora, *J. Geophys. Res., 104*, 24,565.

[14] Evans, JV, 1969. Theory and practice of ionosphere study by Thompson scatter radar, *Proc. IEEE*, *57*, 496-529.

[15] Semeter, JL and F Kamalabadi, 2004. Determination of primary electron spectra from incoherent scatter radar measurements of the auroral E region, *Radio Sci.,* in press.

[16] Lanchester, BS, JR Palmer, MH Rees, D Lummerzheim, K Kaila, and T Turunen, 1993. Energy flux and characteristic energy of an elemental auroral structure, *Geophys. Res. Lett., 21*, 2789.

[17] Hirono, M, 1964. On the observation of the upper atmospheric constituents by laser beams, *J. Radio Res. Lab., 11*, 251-271.

[18] Garner, RC and P Dao, 1995. Molecular nitrogen fluorescence lidar for remote sensing of the auroral ionosphere, *J. Geophys. Res., 100,* 14,131-14,140.

[19] Collins, RL, D Lummerzheim, and RW Smith, 1997. Analysis of lidar systems for profiling aurorally-excited molecular species, *Applied Optics, 36*, 6024-6034, August.

[20] Hedin, AE, 1991. Extension of the MSIS thermospheric model into the middle and lower atmosphere, *J. Geophys. Res.*, *96*, 1159-1172.

[21] Breese, J, 2001. Development of a Fe Boltzmann Temperature Lidar, M.S. Thesis, University of Alaska Fairbanks.

[22] Hou, T, 2002. Development of High Spectral Resolution Iron Boltzmann Lidar, M.S. Thesis, University of Alaska Fairbanks.

[23] Peshave, M, 2004. Design and Implementation of a Microcontroller-Based Closed-Loop Tuning-Controller for a Tunable Dye Laser, M.S. Thesis, University of Alaska, Fairbanks.

[24] Collins, RL, T Hou, MA Peshave, MG Conde, and BW Reinisch, 2003. Observations of Sporadic Sodium-, Iron- and E-Layers at a High-Latitude Site, Fall AGU Meeting, San Francisco, CA, 8-12 December.

[25] Gerstenkorn, S, and P Luc, 1978, *Atlas du Spectre d'Absorption de la Molécule d'Iode entre 14800-20000 cm*$^{-1}$, CNRS, Paris.

[26] Cariou, J, and P Luc, 1980, *Atlas du Spectre d'Absorption de la Molécule Tellure*, CNRS, Orsay.

[27] Chu, X, and GC Papen, 2005, Resonance Fluorescence Lidar for Measurements of the Middle and Upper Atmosphere, in *Laser Remote Sensing*, T Fujii and T Fukuchi eds., Taylor and Francis, Boca Raton.

[28] Romick, GJ, J-H Yee, MF Morgan, D Morrison, LJ Paxton, C-I Meng, 1999, Polar cap optical observations of topside (>900 km) molecular nitrogen ions, *Geophys. Res. Lett*., 26, 1003-1006.

[29] Lehtinen, MS and I Haggstrom, 1987. A new modulation principle for incoherent scatter measurements, *Radio Sci., 22,* 625.

[30] Kelly, JD, CJ Heinselman, JF Vickrey, and RR Vondrak, 1995. The Sondrestrom radar and accompanying ground-based instrumentation, *Space Sci. Rev., 71*, 797.

[31] Farley, DT, 1969. Incoherent scatter correlation function measurements, *Radio Sci., 4,* 935.

[32] Morse, TH and GJ Romick, 1982. The fluctuation and fading of auroral arcs preceding auroral substorm onsets, *Geophys. Res. Lett., 9*, 1065-1068.

[33] Chu, X, G Papen, W Pan, CS Gardner, and J Gelbwachs, 2002. Fe Boltzmann Temperature Lidar: Design, Error Analysis, and First Results from the North and South Poles, *Appl. Opt., 41*, 4400-4410.

[34] Hecht, J, *The Laser Guidebook*, 1992, McGraw-Hill, New York, pp498.

[35] Sherman, J. P., 2002: Mesopause Region Thermal and Dynamical Studies Based on Simultaneous Temperature, Zonal and Meridional Wind Measurements with an Upgraded Sodium Fluorescence Lidar, Ph.D. dissertation, Colorado State University.

Investigating the Auroral Thermosphere with N_2^+ Lidar

Richard L. Collins, Liguo Su, Dirk Lummerzheim
Geophysical Institute
University of Alaska Fairbanks

Richard A. Doe
SRI International

Characterizing the Ionosphere IST-056/RSM-002

June 12, 2006

Fairbanks, Alaska, USA

Lidar or Laser Radar

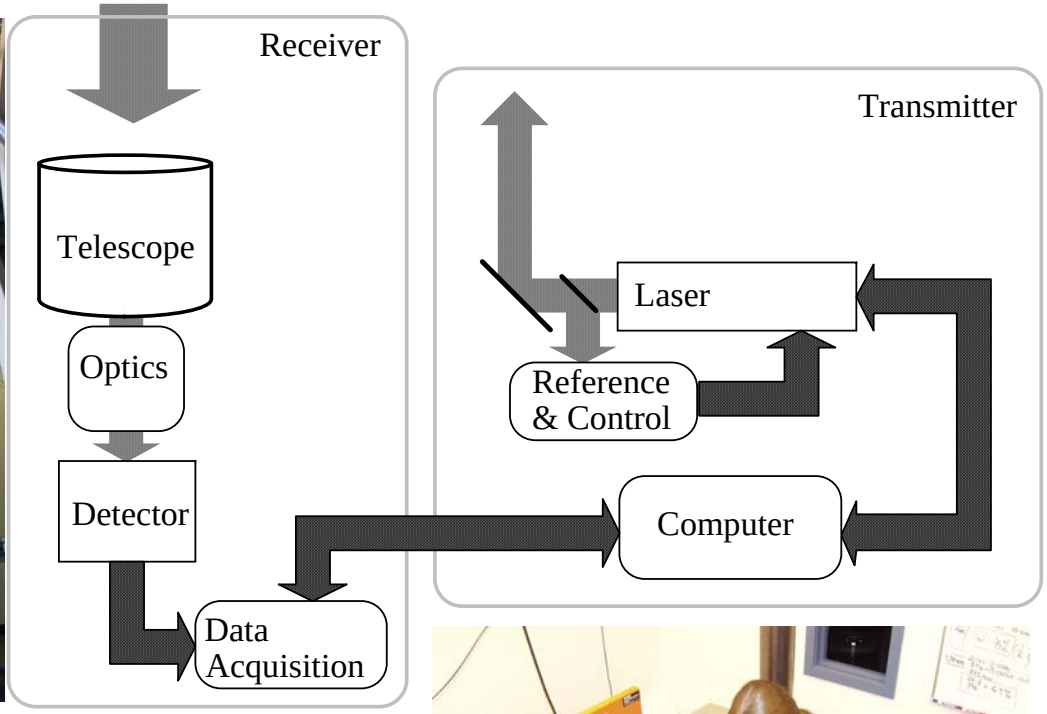

A lidar employs a laser transmitter a telescope receiver and associated control and acquisition systems.

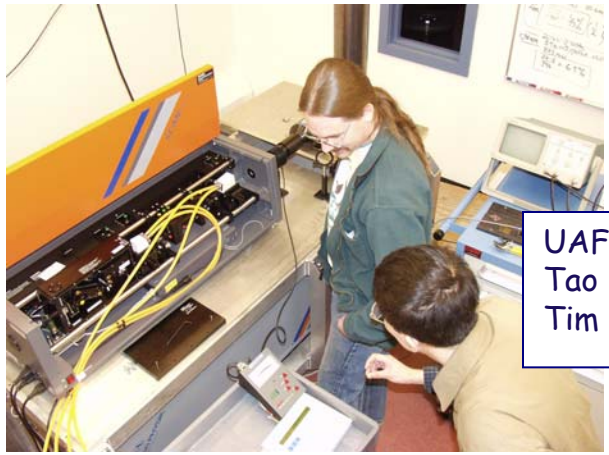

UAF students Tao Hou and Tim Stern.

Atmospheric Lidar Echoes

Light propagates out from the laser and is scattered back into the telescope.

The scattering mechanisms include;

- Mie Scatter
- Rayleigh Scatter
- Resonance Scatter
- Raman Scatter

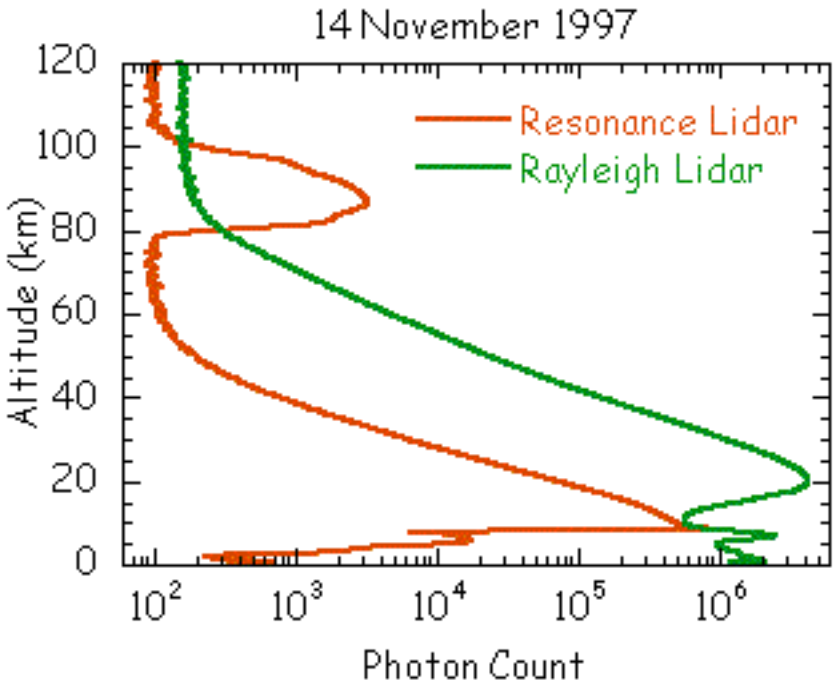

Rayleigh and resonance lidar signals plotted as a function of altitude.

Lidar Equation

Number of photons transmitted

Probability of scattered photon being detected

$$N(z) = (\eta\, T)\left(\frac{E_L R_L \Delta t}{(hc/\lambda_L)}\right)(\sigma_{eff}\, \rho(z)\Delta z)\left(\frac{A}{4\pi z^2}\right) + N_B R_L \Delta t(2\Delta z / c)$$

Efficiency

Probability of photon being scattered

Background Light - Noise

η	lidar receiver efficiency
T	two way atmospheric transmission
E_L	energy per pulse (J)
R_L	laser repetition rate (s^{-1})
Δt	observation interval (s)
h	Planck's constant (6.63 x 10^{-34} J/s)
c	speed of light (3.00 x 10^8m/s)
λ_L	transmitted wavelength (m)
σ_{eff}	effective backscatter cross section (m^2)
$\rho(z)$	density of scatterers (m^{-3})
Δz	receiver range bin length (m)
A	receiver telescope area (m^2)
N_B	background light emission rate (photon/sec)

How Much Rayleigh Signal ?

Consider a Rayleigh lidar system transmitting 1 J pulses of radiation into the sky at 532 nm and receiving the backscattered light back with a 1-m telescope at 10, 30, 60, 90 and 120 km.

$\blacklozenge_{eff}$	10^{-32} m^2
$\rho(z)$	10^{25} m^{-3}, 10^{24} m^{-3}, 10^{22} m^{-3}, 10^{20} m^{-3}, 10^{18} m^{-3}
Δz	1 km
Efficiency	5%
Scattering probability	10^{-3}, 10^{-5}, 10^{-7}, 10^{-9}, 10^{-11}
Receiver probability	8×10^{-9}, 9×10^{-10}, 2×10^{-10}, 10^{-10}, 5×10^{-11}

Transmitted Signal

Photons per pulse 3×10^{18}

Expected Signal

~ 12×10^{5} photons/pulse at 10 km
~ 14×10^{2} photons/pulse at 30 km (1:860)
~ 3.0 photons/pulse at 60 km (1:470)
~ 15×10^{-3} photon/pulse at 90 km (1:200)
~ 75×10^{-6} photon/pulse at 120 km (1:200)

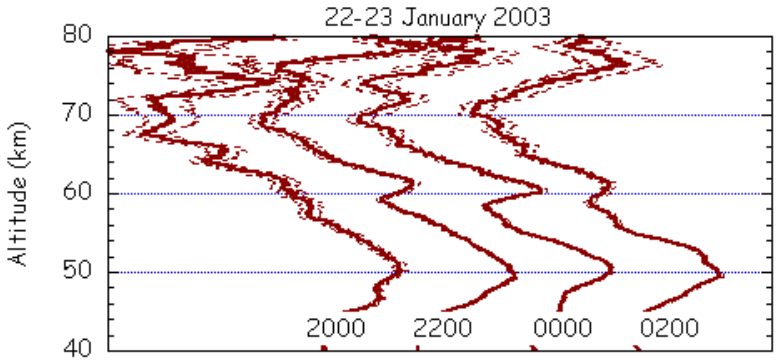

Temperature profiles measured with Rayleigh lidar at Poker Flat Research Range.

How Much Resonance Signal ?

Consider a Sodium Resonance lidar system transmitting 10 mJ pulses of radiation into the sky at 589 nm and receiving the backscattered light back with a 1-m telescope at 90 km.

$\blacklozenge_{eff}$	10^{-16} m^2 (10^{-32} m^2)
$\rho(z)$	10^{10} m^{-3} (10^{20} m^{-3})
Δz	1 km
Efficiency	5%
Scattering probability	10^{-3} (10^{-9})
Receiver probability	10^{-10} (10^{-10})

Transmitted Signal

Photons per pulse 3×10^{16} (3×10^{18})

Expected Signal

~ 150 (15×10^{-3}) photon received per pulse at 90 km (10000:1)

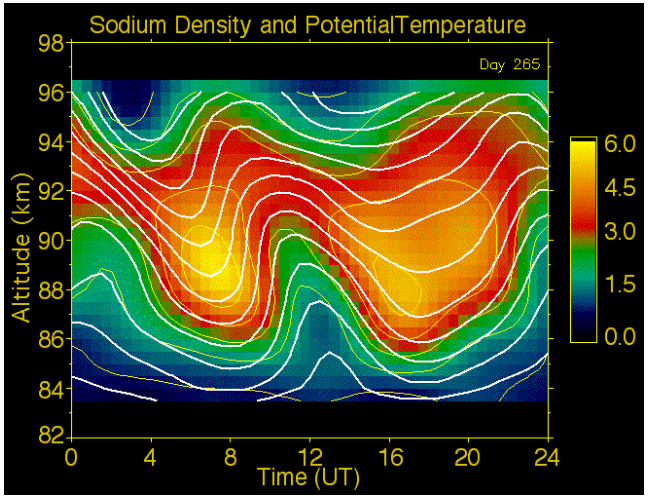

Sodium Density and Potential Temperature measured by Resonance Lidar at Colorado State University, Fort Collins, CO, USA.

Why Do Signal Levels Matter ?

The fundamental uncertainty in the measurement

$$\Delta N(z) = (N(z))^{1/2}$$

- arises due to the statistical nature of the detection process - Poisson Statistics.

A signal level of 100 photon counts has an inherent uncertainty of 10 photon counts or 10%.

- However, if a signal of 100 photon counts is accompanied by a background of 9900 photon counts yielding a total uncertainty of $(100+9900)^{1/2} = 100$ and therefore a relative uncertainty of 100%.

- To increase a signal quality by 10 requires we increase a signal magnitude by 100.

- We can play with Δz and Δt to get a given measurement quality

- **** Resolution vs. Accuracy ****

The Ionosphere and Thermosphere

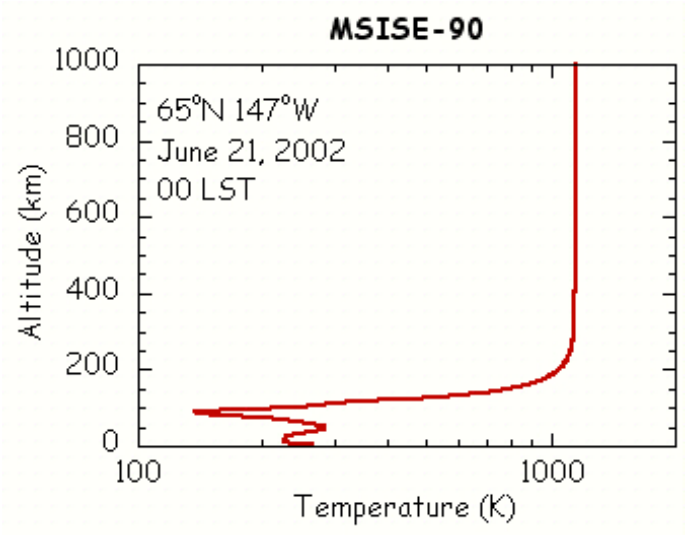

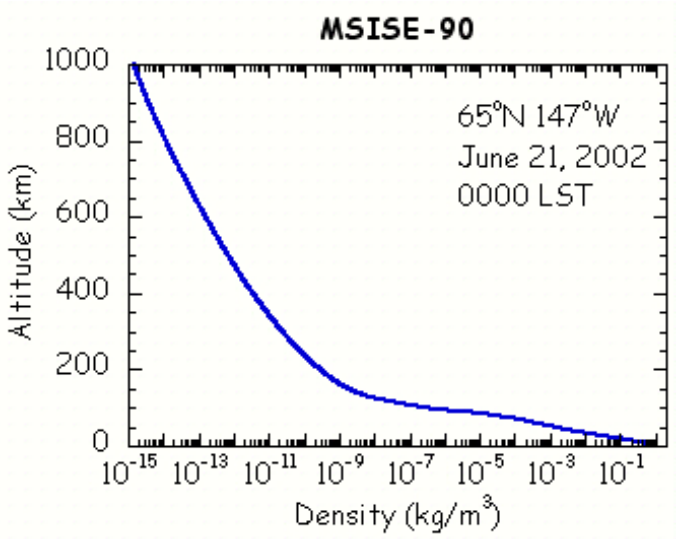

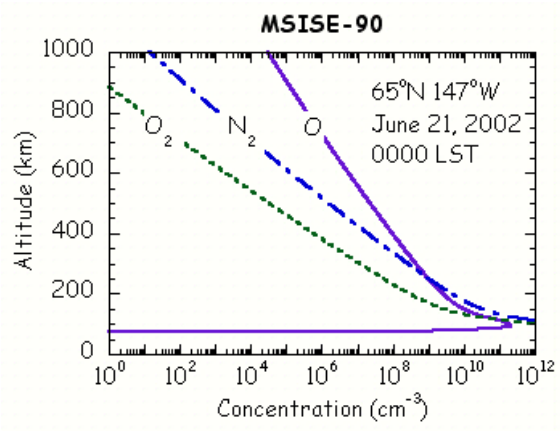

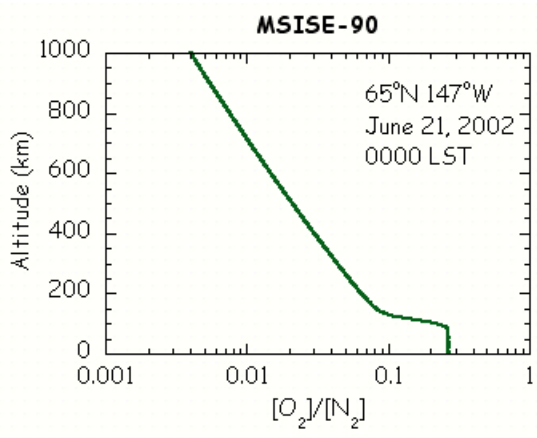

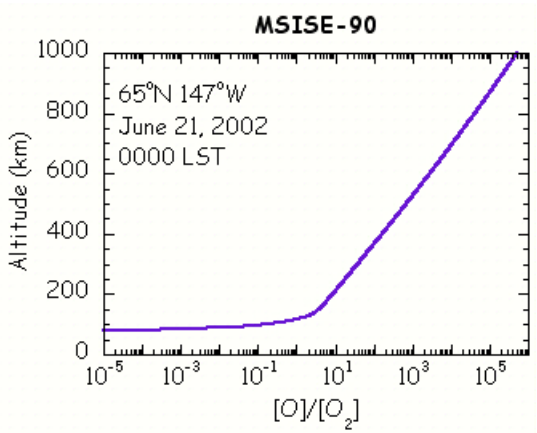

The Aurorally-Modified Ionosphere

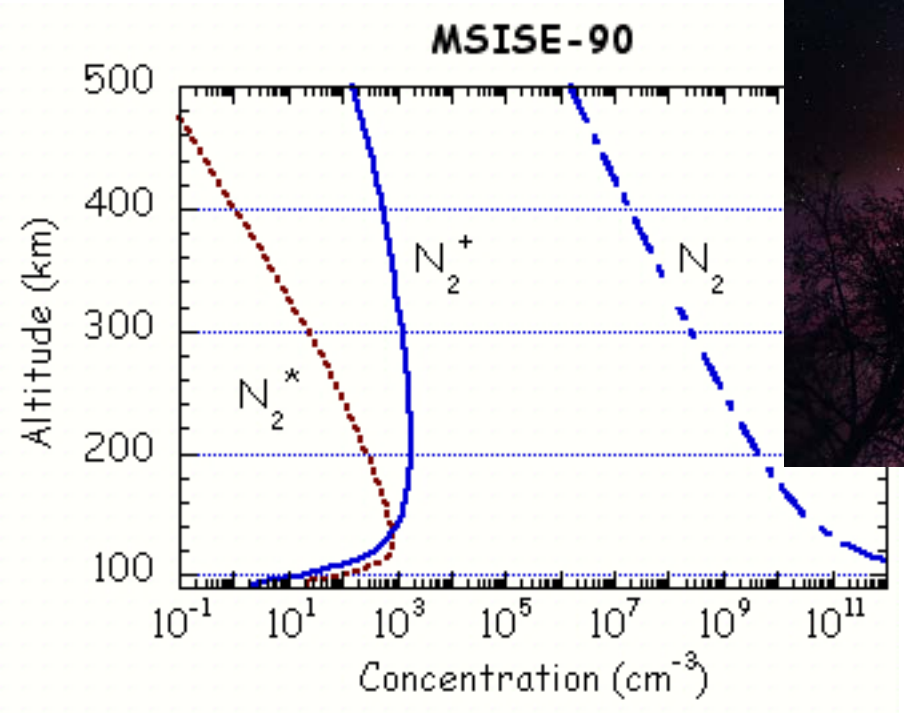

Photo courtesy of GI-UAF by Jan Curtis

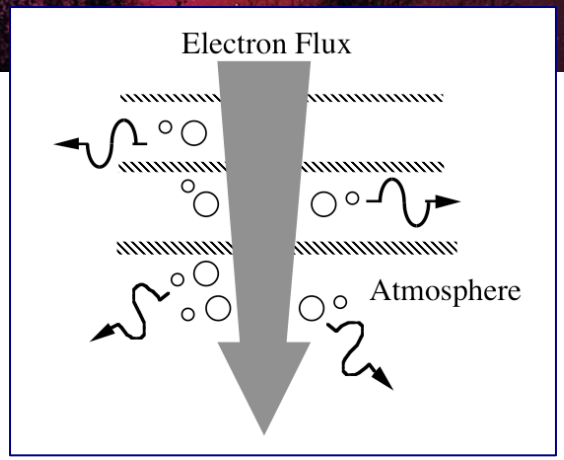

The aurora modifies the composition of the ionosphere.

The Spectroscopy of Molecular Nitrogen

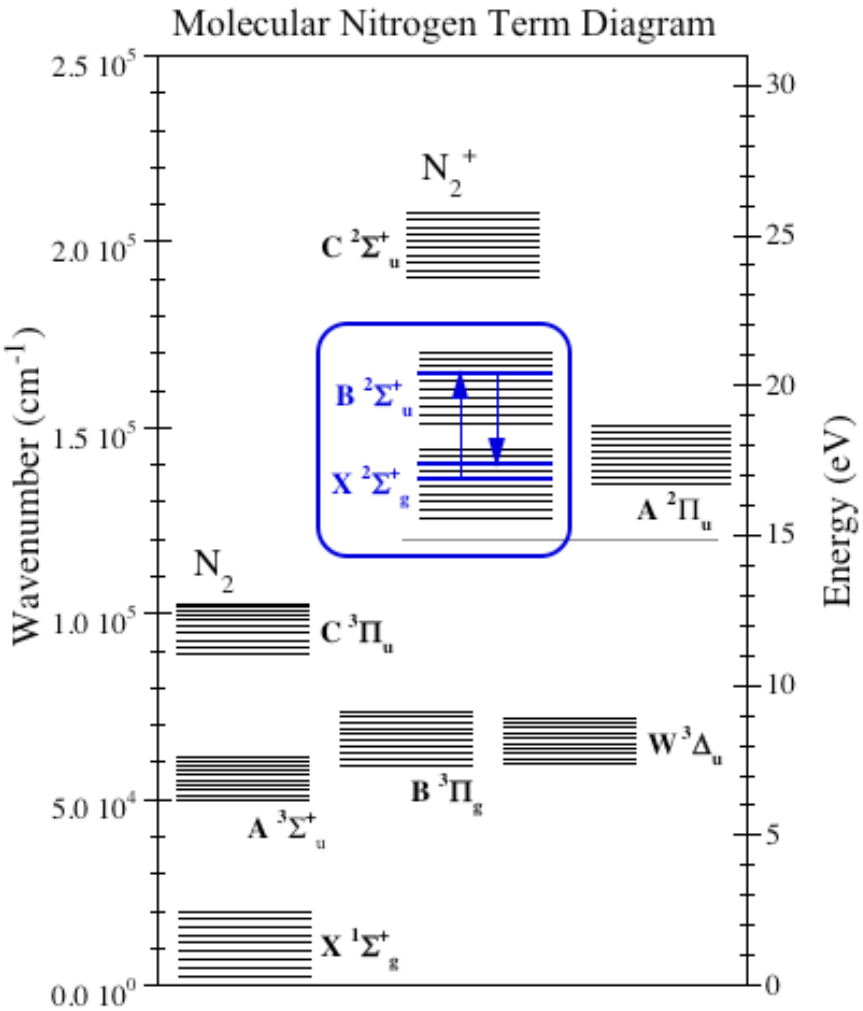

Partial term diagram for molecular Nitrogen. Transitions of interest include

$N_2(A^3\Sigma^+_u) \rightarrow N_2(B^3\Pi_g)$

the "first positive" system

$N_2(B^3\Pi_g) \rightarrow N_2(C^3\Pi_u)$

the "second positive" system, and

$N_2^+(X^2\Sigma^+_g) \rightarrow N_2^+(B^3\Sigma^+_u)$

the "first negative" system.

Choosing an Viable Scatterer

The "first negative" transitions (i.e., $N_2^+ (X^2\Sigma^+_g) \rightarrow N_2^+(B^3\Sigma^+_u)$) have a significantly higher Einstein A-Coefficient than the "first positive" transitions (i.e., $N_2(A^3\Sigma^+_u) \rightarrow N_2(B^3\Pi_g)$) and the "second positive" transitions (i.e., $N_2(B^3\Pi_g) \rightarrow N_2(C^3\Pi_u)$).

For N_2^+, $\sigma_{eff} \sim 5 \times 10^{-18}$ m^2 (10^{-16} m^2 for Na)

The chosen vibrational transition (■ = 0 ✹ ■ = 0 ✹ ■ = 0) is 2.4 times more optically efficient than the next most efficient transition (■ = 2 ✹ ■ = 3 ✹ ■ = 2).

The excited oxygen transition $O(^3P) \rightarrow O(^3S^0)$ at 844.65 nm has been observed but the lower state (i.e., $O(^3S^0)$) is very short-lived (~5 ns) and not a suitable lower state for lidar observations .

The Spectroscopy of Molecules vs. Atoms

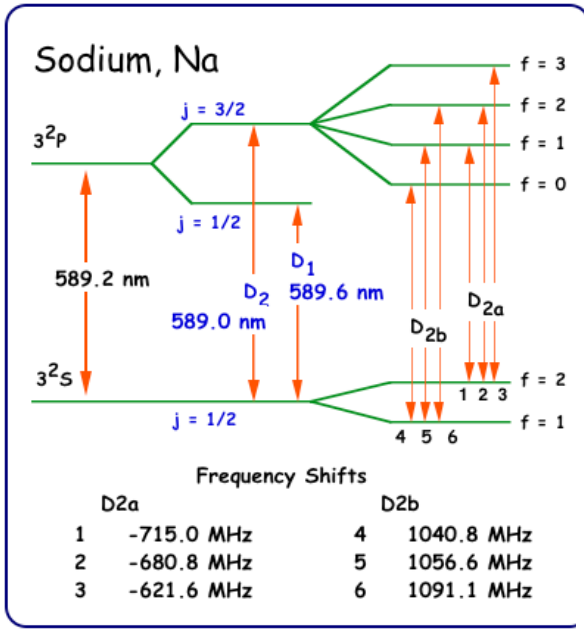

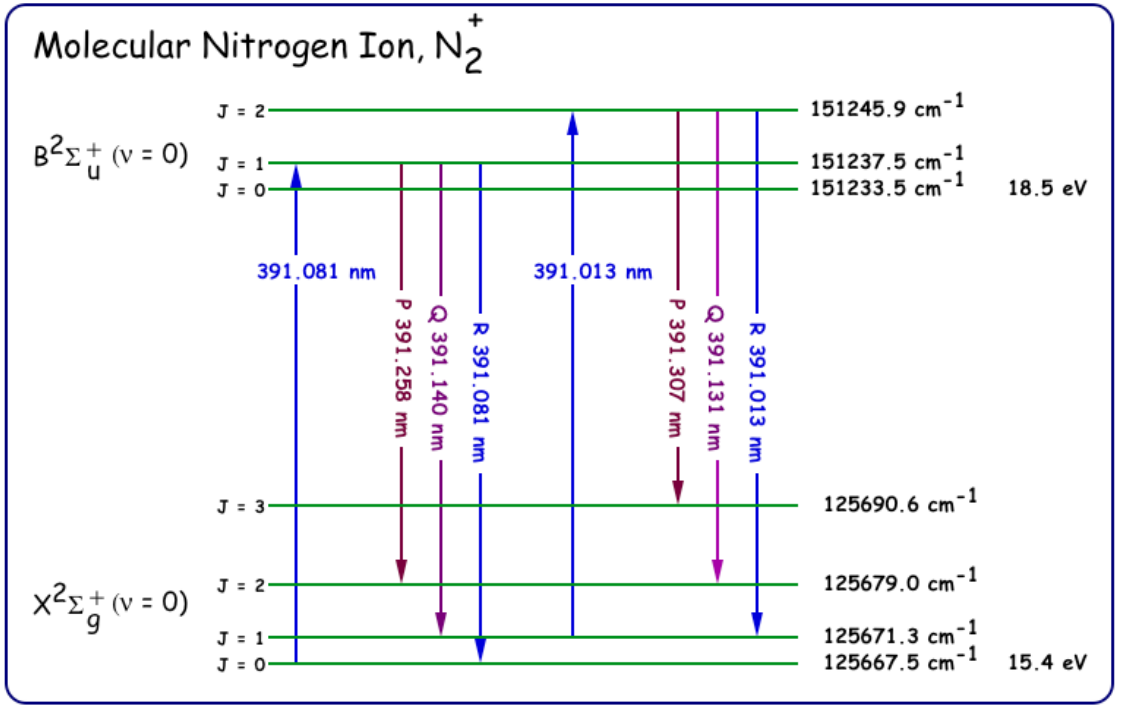

Molecular spectroscopy has vibrational and rotational states.

Rotational Population

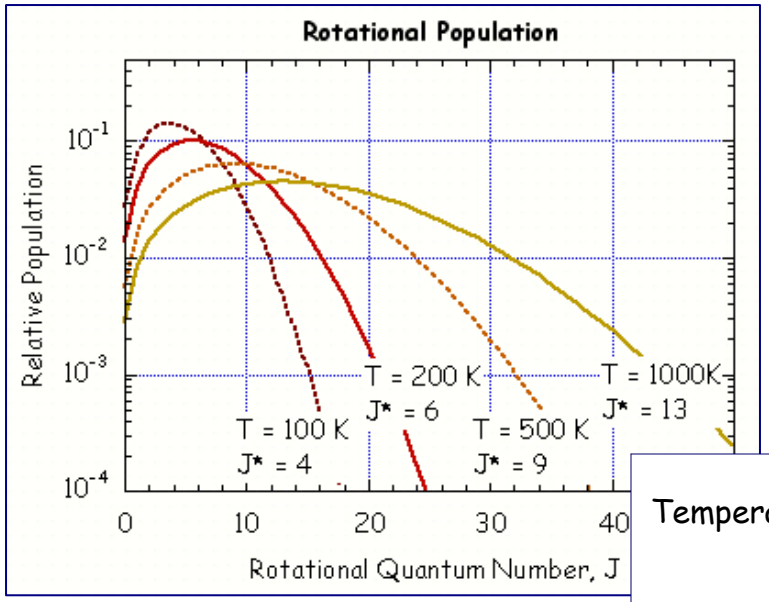

The optimum lidar wavelengths vary with rotational population.

Temperature	J	Relative Population	Transmit Wavelength	Receive Wavelength
100 K	4	14%	390.781 nm	391.428 nm
200 K	6	10%	390.604 nm	391.486 nm
500 K	9	6.4%	390.303 nm	391.537 nm
1000 K	13	4.5%	389.839 nm	391.541 nm

Simulation of a Case Study

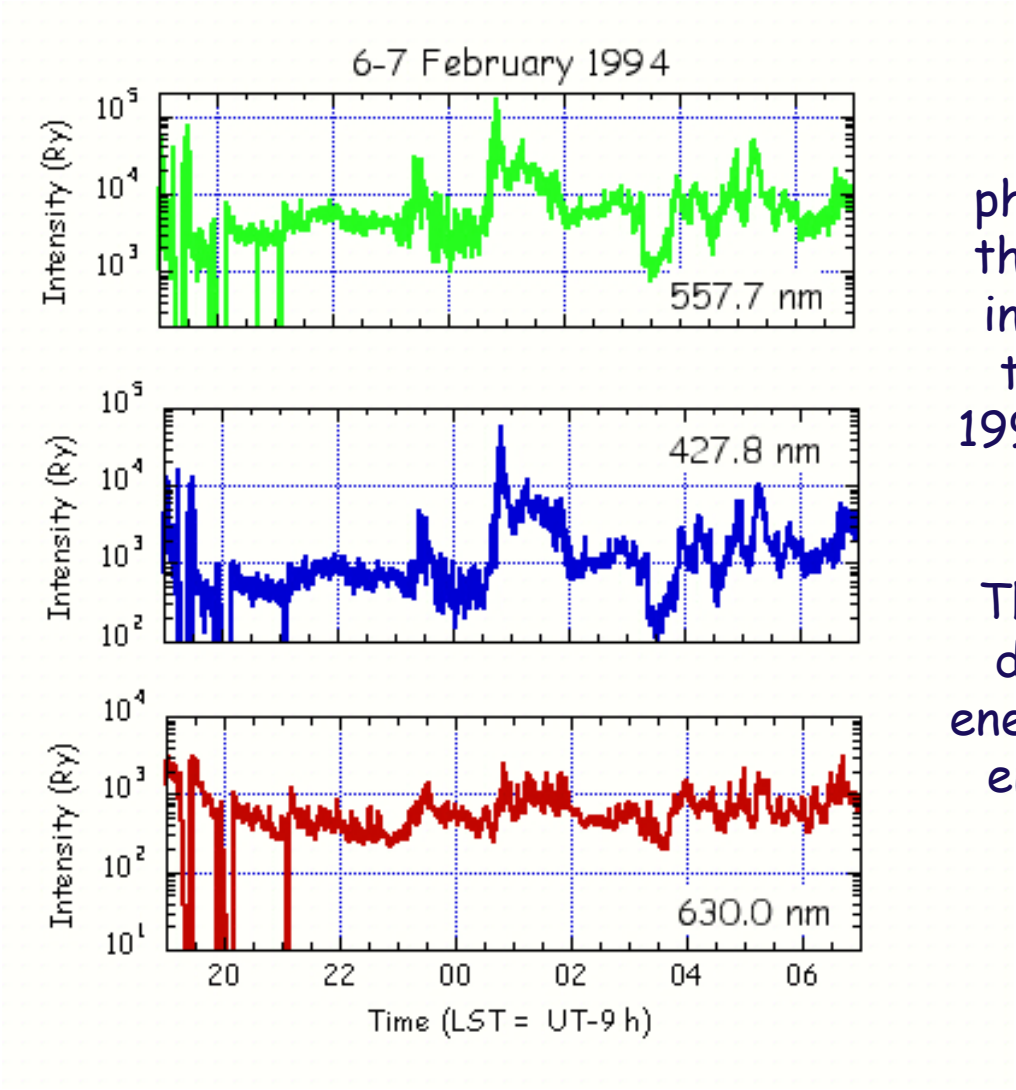

A meridian scanning photometer (MSP) recorded the intensity of the skylight in the magnetic meridian on the night of 6-7 February 1994 during moderate auroral activity.

The MSP observations allow determination of the total energy flux and characteristic energy of the precipitating particles

Estimating Concentrations of N_2^+

The results of the MSP analyses are input into a model that simulates the aurorally-modified atmosphere. The model estimates the distribution of molecular nitrogen ions

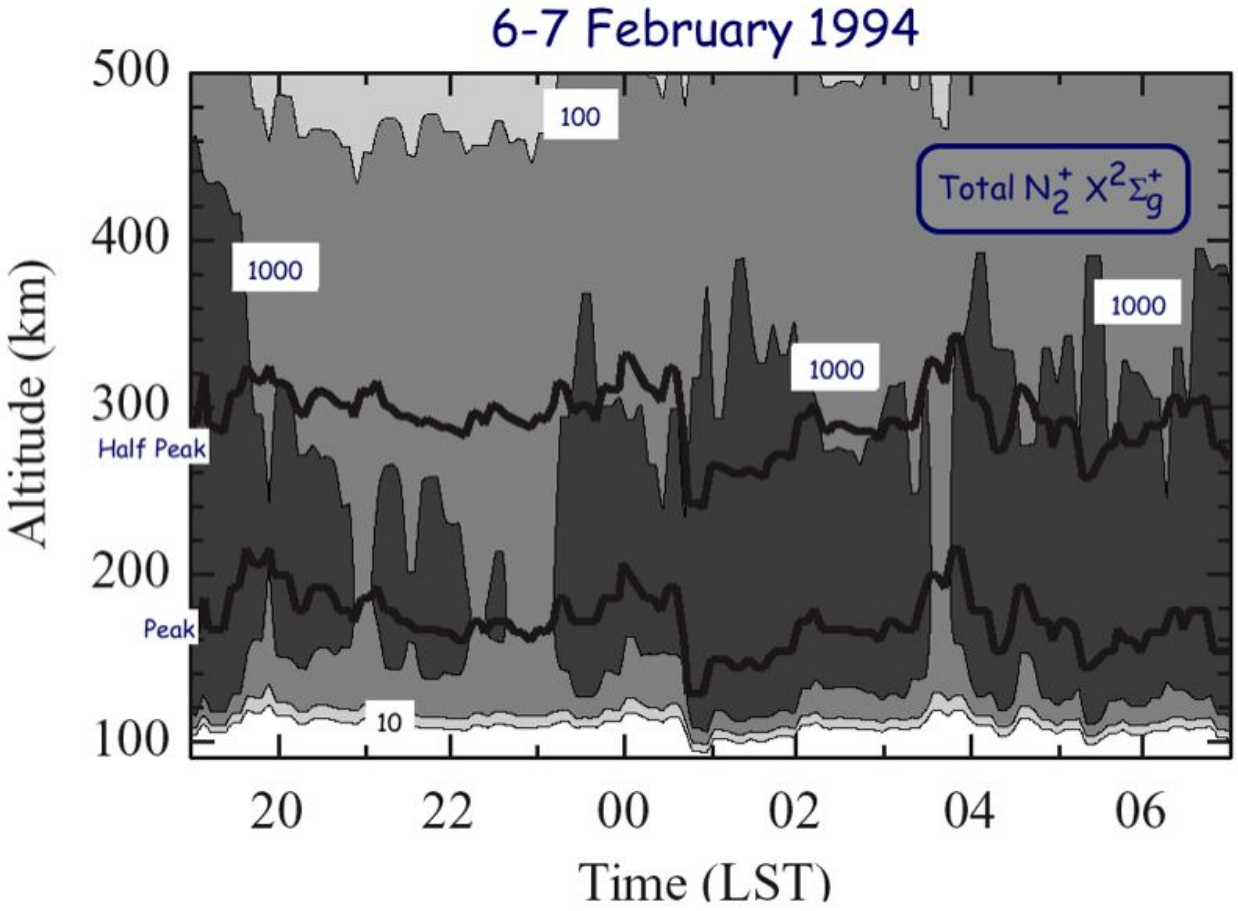

A Prototype Lidar System

Proposed N_2^+ XB Lidar System

Transmitter		Receiver	
Laser	Excimer-pumped Dye	Telescope Diameter	1 m
Pulse Energy	50 mJ	Detector	Photomultiplier Tube
Pulse Repetition Rate	20 pps	Filter Bandwidth	0.3 nm
Wavelength	390.303 nm	Wavelength	391.537 nm
Measurement Resolution			
Temporal Resolution	300 s		
Spatial Resolution	5 km		

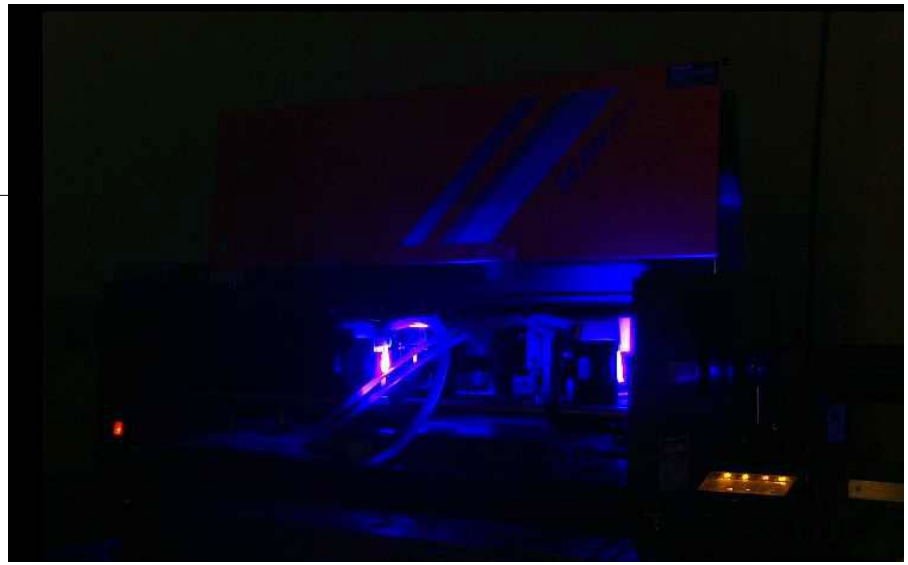

Lidar Performance

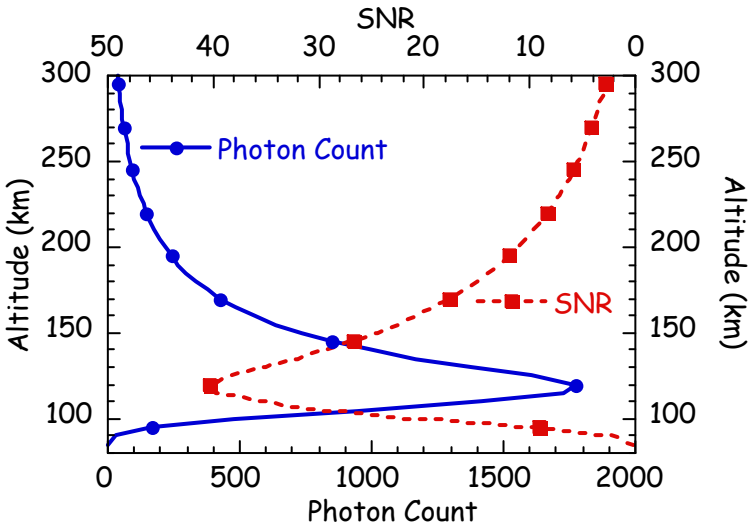

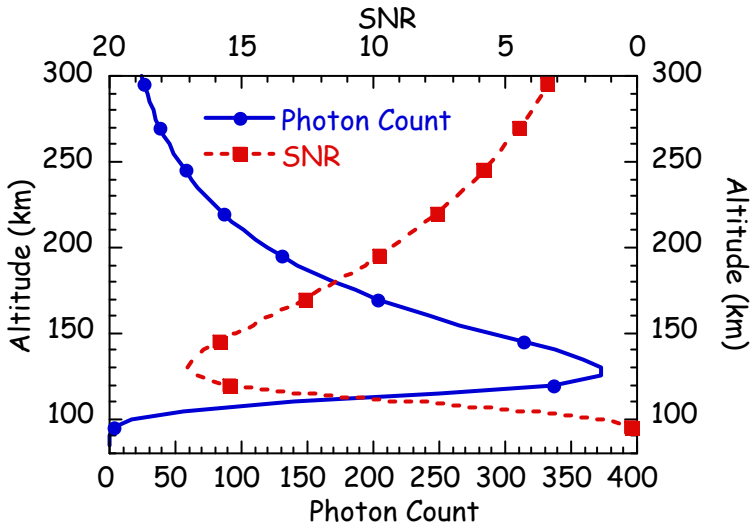

The expected signal varies with auroral activity. The best measurements are made near 0057 LST. However, the lidar system is capable of making measurements throughout the night.

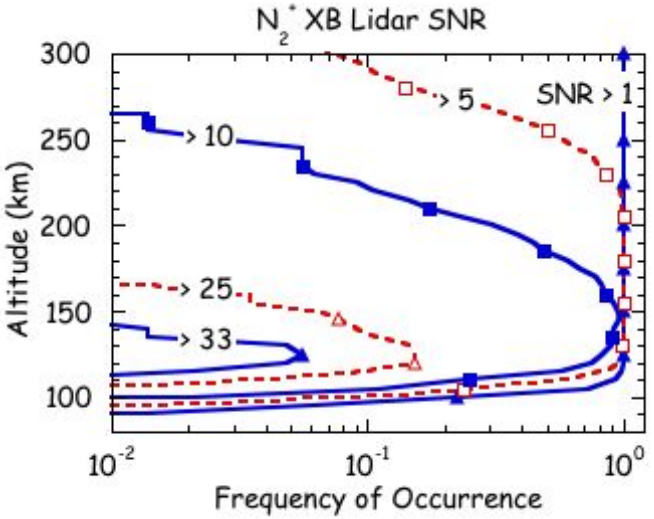

The Advanced Modular Incoherent Scatter Radar (AMISR)

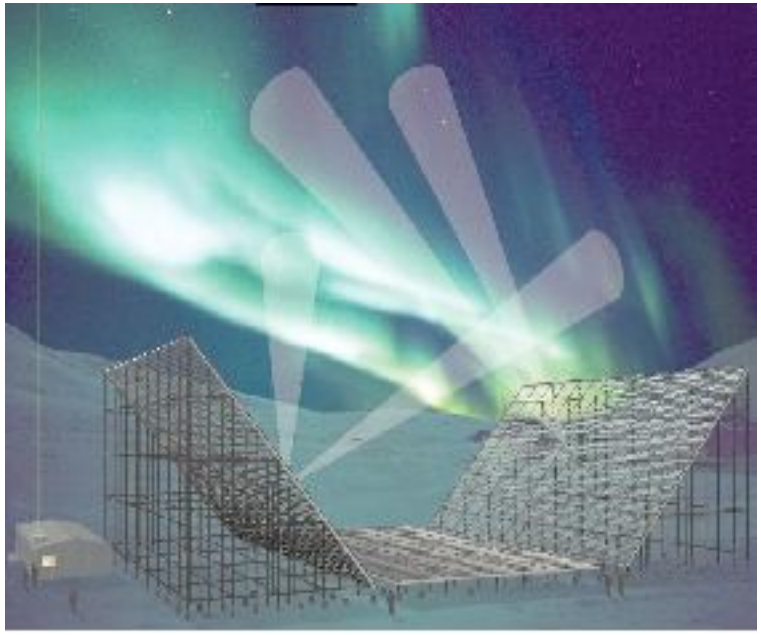

Lidar measurements of N2+ will be nested within the AMISR measurements of the total plasma.

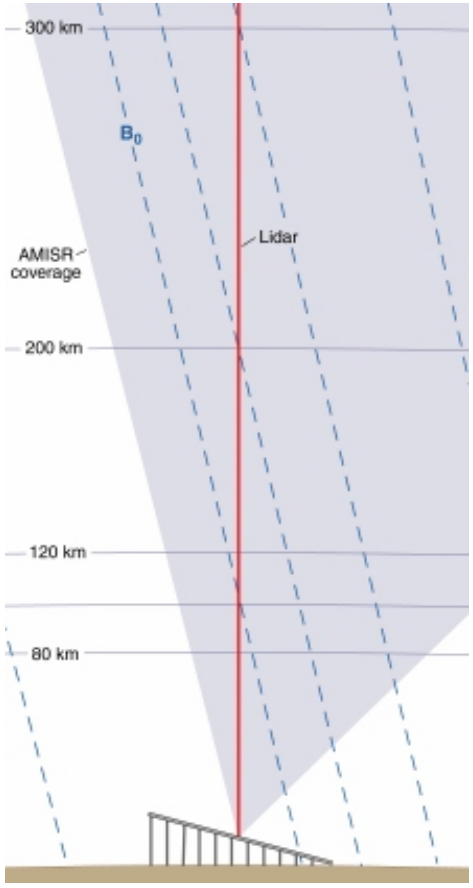

Combined Measurements

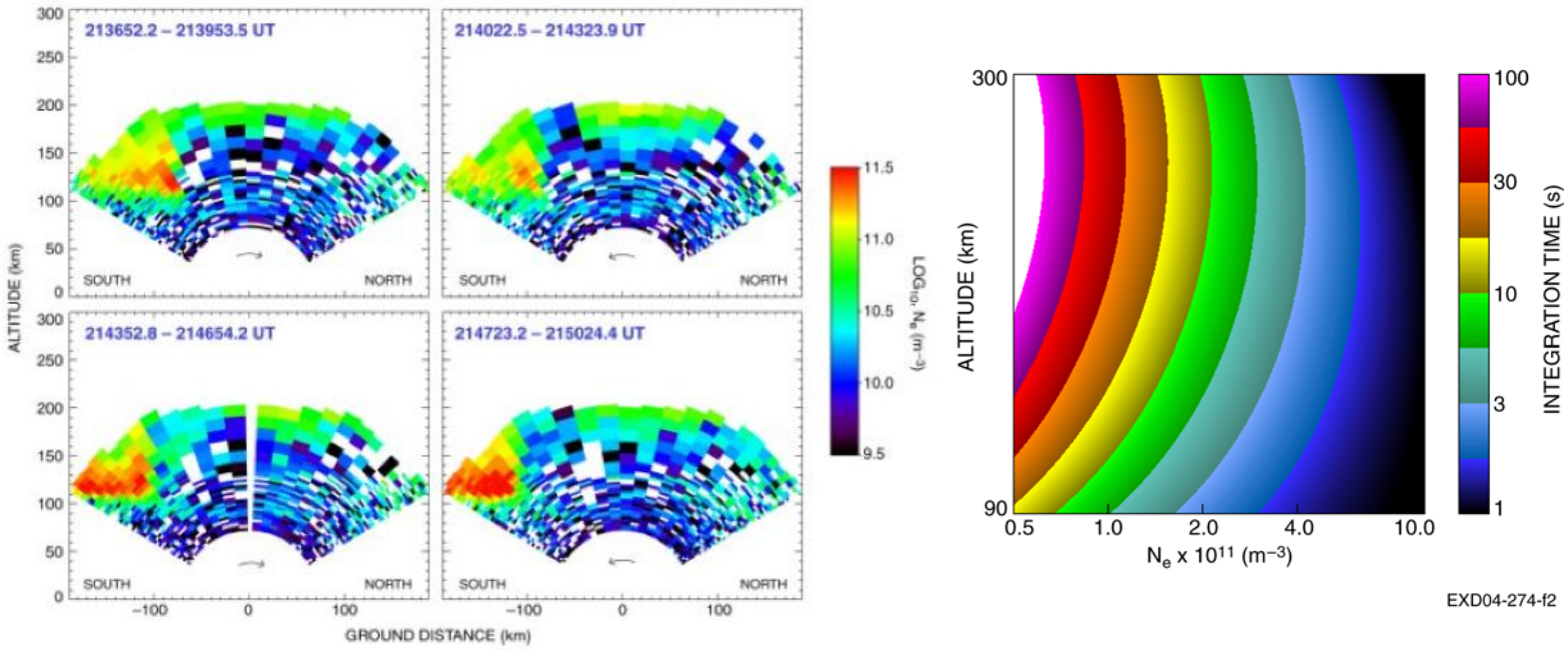

For ionization densities of 4x105 cm-3 at 115 km AMISR will make 10% measurements at 3 km resolution every 2 seconds while the N2+ lidar will make 10% measurements at 1 km resolution every 30 seconds.

E-Region Chemical Assimilation

1. $\eta_{N_2^+} = [N_2^+](\gamma_3[O_2] + (\gamma_4 + \gamma_{19})[O])$

2. $\eta_{O_2^+} + \gamma_5[N_2^+][O_2] = (\gamma_{15}[NO] + \gamma_8[N_2] + \alpha_1 n_e)[O_2^+]$

3. $\gamma_4[N_2^+][O] + \gamma_8[O_2^+][N_2] + \gamma_{15}[O_2^+][NO] = \alpha_3 n_e[NO^+]$

4. $n_e = [NO^+] + [O_2^+] + [N_2^+]$

MSP | Lidar | Radar | Chemistry Model | MSIS

Solve for N_2^+, O_2^+, NO^+ and NO.

Beyond Concentration Profiling

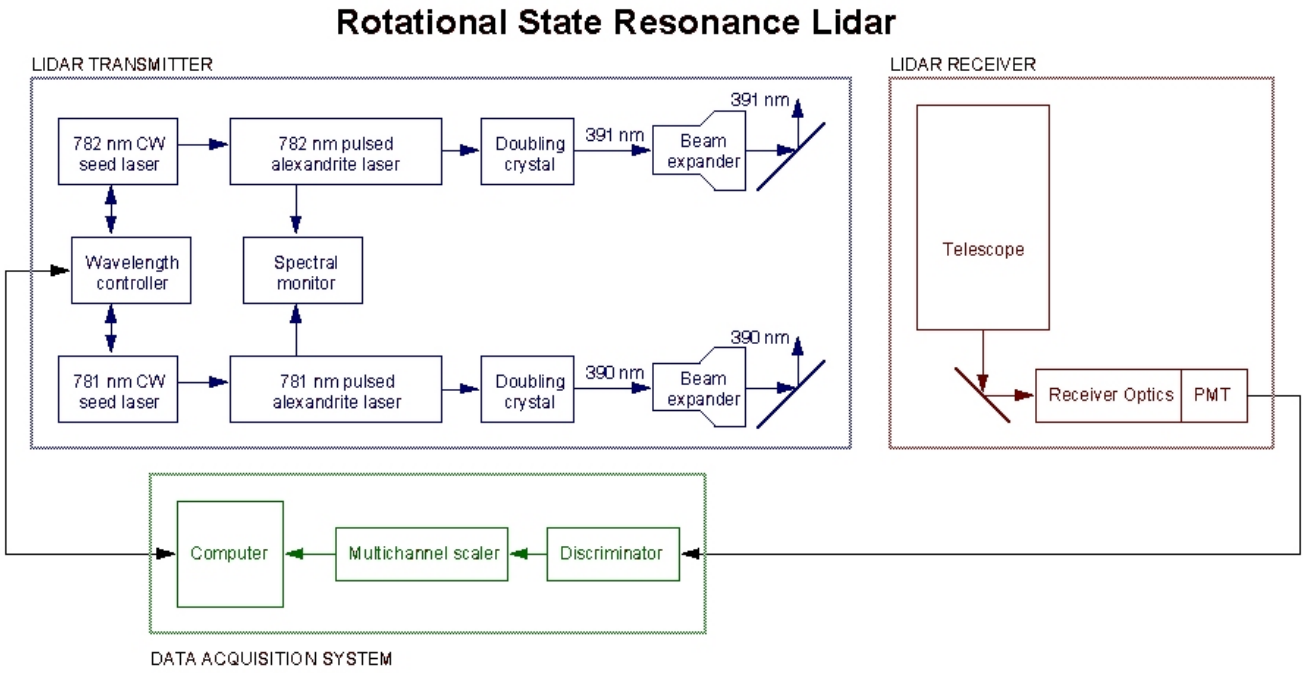

A dual laser lidar system employing solid-state lasers could be used to profile two rotational states simultaneously and hence study the energy deposition in the auroral ionosphere.

Conclusions and Discussion

N_2^+ lidar appears feasible for studies of the auroral thermosphere.

Range-resolved measurement of a specific ion extends the scope of current radar/photometer experiments.

The lidar differs in several technical aspects from "traditional" atomic resonance lidars.

Operational techniques will be developed to yield robust lidar measurements.

Assimilation techniques will be developed to yield robust retrievals of ionospheric species.

Acknowledgements

The current N_2^+ lidar is being developed at the Lidar Research Laboratory (www.gi.alaska.edu/splidar) , Poker Flat Research Range with support from the US National Science Foundation under grant ATM-05-14103.

The authors acknowledge the on-going operational support of the staff at Poker Flat Research Range.

The Advanced Modular Incoherent Scatter radar is currently being deployed at Poker Flat Research Range with support from the US National Science Foundation.

Poker Flat Research Range is operated by the Geophysical Institute of the University of Alaska Fairbanks with support from the US National Aeronautics and Space Administration.